

# Diffusional Instabilities on Curved Manifolds

by

Henry Shackleton

Submitted to the Department of Physics  
in partial fulfillment of the requirements for the degree of

Bachelor of Science

at the

MASSACHUSETTS INSTITUTE OF TECHNOLOGY

June 2018

© Massachusetts Institute of Technology 2018. All rights reserved.

## Signature redacted

Author .....

✓ Department of Physics  
May 11, 2018

## Signature redacted

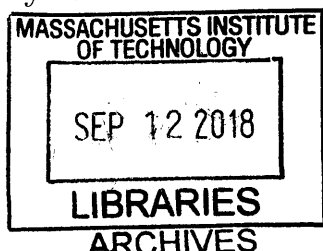
Certified by .....

Mehran Kardar  
Professor of Physics  
Thesis Supervisor

## Signature redacted

Accepted by .....

✓ Professor Scott Hughes  
Interim Physics Associate Head, Department of Physics





# **Diffusional Instabilities on Curved Manifolds**

by

Henry Shackleton

Submitted to the Department of Physics  
on May 11, 2018, in partial fulfillment of the  
requirements for the degree of  
Bachelor of Science

## **Abstract**

Diffusionally-driven instabilities provide a versatile mechanism for pattern formation, and have found applications in modeling a variety of biological and chemical systems. Although pattern formation has been observed in systems with a variety of geometries, the theoretical study of diffusional instabilities has primarily been restricted to systems of uniform curvature, such as flat planes, spheres, and cylinders. In this thesis, I study a method of analyzing pattern formation on more generally deformed surfaces, with a focus on perturbatively calculating effects due to small deformations from geometries of uniform curvature. Analytical predictions, ranging from pattern modifications to pinning of pattern development, are obtained on deformed drums, cylinders, and spheres. These predicted effects are compared to numerical studies, and additional cases where our analytical methods break down are studied numerically. Finally, the interplay between advection and non-uniform curvature is studied numerically.

Thesis Supervisor: Mehran Kardar  
Title: Professor of Physics



## Acknowledgments

As is the case with most (all?) physicists, I would not be where I am today without the help and support of many people. I hope that my gratitude has been sufficiently expressed in person such that an acknowledgment in a thesis is not necessary for you to recognize my thanks, but for completeness, here they are.

My primary thanks go to the collaborators and advisers who made this project possible - Professors Kardar, Guven, and John Frank. The formalism described in Chapter 3 was developed by Professor Guven, and John laid the framework necessary for the necessary numerical studies of this project. Additional thanks is extended to Professor Kardar who, through a combination of teaching and research advising, has likely had the largest impact on my development and goals as a physicist.

I am grateful to my physicist peers - Caitlin, Rudy, Adin, Patrick, and many others - for helping me in countless ways through my undergraduate career.

This work was supported partly by the MIT UROP program, who bore with my constant inability to turn in timesheets.

Finally, to Sam. Your support, both as a physicist and as a friend, got me to where I am today. Thank you.



# Contents

<b>1</b>	<b>Introduction</b>	<b>15</b>
1.1	Overview and Motivation . . . . .	15
1.2	Thesis Structure . . . . .	17
<b>2</b>	<b>Pattern Formation in Reaction-Diffusion Systems</b>	<b>19</b>
2.1	Linear Stability Analysis of Reaction-Diffusion Systems . . . . .	19
2.2	Geometric Dependence of Pattern Formation . . . . .	21
2.2.1	Pattern Changes . . . . .	21
2.2.2	Symmetry Breaking . . . . .	22
2.2.3	Instability through Spectrum Shifts . . . . .	22
2.2.4	Non-Linear Effects . . . . .	23
<b>3</b>	<b>Laplacian Modifications From Geometric Perturbations</b>	<b>25</b>
3.1	Developing a Perturbation Theory via Conformal Mapping . . . . .	25
3.1.1	Perturbations of a Flat Planar Drum . . . . .	26
3.1.2	Perturbations from a Uniform Cylinder . . . . .	29
3.1.3	Perturbations from a Uniform Sphere . . . . .	31
<b>4</b>	<b>Geometric Modifications of Turing Patterns</b>	<b>33</b>
4.1	Gaussian Deformations of a Drum . . . . .	33
4.1.1	Eigenvalue Modifications . . . . .	33
4.1.2	Turing Pattern Modifications . . . . .	34
4.2	Gaussian Deformations of a Cylinder . . . . .	36

4.2.1	Eigenvalue Modifications . . . . .	36
4.2.2	Turing Pattern Modifications . . . . .	39
4.3	Periodically Rippled Cylinder . . . . .	41
4.3.1	Eigenvalue Modifications . . . . .	41
4.3.2	Turing Pattern Modifications . . . . .	42
4.4	Gaussian Deformations of a Sphere . . . . .	43
4.4.1	Eigenvalue Modifications . . . . .	43
4.4.2	Turing Pattern Modifications . . . . .	43
<b>5</b>	<b>Time-Dependent Turing Patterns</b>	<b>47</b>
5.1	Introduction to Reaction-Advection-Diffusion Systems . . . . .	47
5.2	Linear Stability Analysis of Reaction-Advection-Diffusion Systems . .	48
5.3	Conformal Mapping the Advection Operator . . . . .	50
5.4	Advection on a Deformed Cylinder . . . . .	50
5.4.1	Analytical Restrictions . . . . .	50
5.4.2	Numerical Results . . . . .	51
<b>6</b>	<b>Conclusion</b>	<b>53</b>
<b>A</b>	<b>Rayleigh-Schrödinger Perturbation Theory for Momentum-Dependent Potentials</b>	<b>55</b>
A.1	Problem Statement . . . . .	55
A.2	First Order Corrections . . . . .	56
A.2.1	Non-Degenerate Perturbation Theory . . . . .	56
A.2.2	Degeneracy Effects . . . . .	57
A.3	Higher Order Corrections . . . . .	57
<b>B</b>	<b>Details of Numerical Simulations</b>	<b>59</b>

## List of Figures

4-3 (Left) The first-order eigenvalue corrections for the symmetric and antisymmetric modes, plotted as a function of wavelength $\ell$ relative to the standard deviation of the Gaussian bump $\sigma$ . (Right) The eigenfunction that receives the largest first-order correction compared with the width of the Gaussian bump. The wavelength of this eigenfunction is approximately twice the width of the bump. . . . .	38
4-4 (Left) The degeneracy of the allowed eigenmodes on a cylinder is broken by the Gaussian bump, splitting into symmetric and antisymmetric modes, labeled by green and red points. In the context of Turing patterns, one of these modes is closest to the most unstable mode, $k^*$ , and hence dominates the resulting pattern. (Right) Patterns from the Thomas-Murray reaction-diffusion model in Eq.4.2 are entrained to a Gaussian bump, switching in phase between inward and outward deformations. . . . .	39
4-5 Near critical reaction-diffusion equations on geometries with large deformations can lead to localization of the resulting Turing patterns (top), although this phenomenon is sensitive to boundary effects and length scales (bottom). . . . .	40
4-6 (Left) Periodic rippling creates a band gap in the Laplacian spectrum (blue), which in turn creates a similar gap in the Turing dispersion relation (green). This leads to the most unstable mode switching sharply between cosine and sine as the mode is dialed past $p/2$ . (Right) Numerical simulations of the Thomas-Murray model in COM-SOL Multiphysics®, where concentrations switch from troughs to ridges as the most unstable mode passes $p/2$ . . . . .	42

- 4-7 (Left) First-order Laplacian eigenvalue corrections from two Gaussian deformations on either pole of a sphere as a function of the width of the deformation, for  $\ell = 1 - 5$ . These corrections increase monotonically both in the width of the bump and in the order of the eigenfunction. (Right) First-order Laplacian eigenvalue corrections normalized by their base eigenvalue,  $\lambda_{\ell m}^{(0)}$ . . . . . 44
- 4-8 (Top) Spotted patterns from the Thomas-Murray reaction-diffusion model on deformed spheres can be entrained to deformations, possibly prevented by incommensurability of length scales and nonlinear interactions. (Bottom) In the initial development of Turing patterns, an undeformed sphere presents diffusionaly-unstable modes corresponding to the eigenfunction  $Y_5^5$ . Upon introducing inward deformations, the diffusion rate of lower harmonics is increased, thus causing the  $Y_3^0$  pattern to become diffusionaly unstable. . . . . 45
- 5-1 The velocity of the propagation of Turing patterns in a reaction-advection-diffusion system on a deformed cylinder, normalized by the advection rate  $a_1 = a_2 = a$ . Inward Gaussian deformations speed up the rate of propagation, whereas outward Gaussian deformations slow it down, potentially stopping the flow of the pattern all together. A slight dependence on the width of the deformation  $\sigma$  is also observed, suggesting that deformations with larger curvature modify propagation speed more. 52



# List of Tables

B.1 A list of parameters used in the numerical simulations included in this thesis. . . . .	60
---	----



# Chapter 1

## Introduction

### 1.1 Overview and Motivation

In 1952, Alan Turing noted that two chemicals undergoing a combination of diffusion and a chemical reaction - mechanisms that independently led to homogeneous distributions of chemicals - could together form areas of high and low concentration [2]. Stated more generally, a multicomponent *reaction-diffusion* system, or systems with two or more variables  $\mathbf{C}(x, t)$  obeying the equation

$$\frac{\partial \mathbf{C}}{\partial t} = \nabla^2 \mathbf{C} + \mathbf{R}(\mathbf{C}), \quad (1.1)$$

where  $\nabla^2$  is the Laplacian operator and  $\mathbf{R}(\mathbf{C})$  is a reaction term, can have position-dependent steady-state solutions. Eq. 1.1 is a natural way to describe a large number of processes in nature, including features of biological and chemical systems. As such, Turing's observation provided a natural way in which the development of spatial inhomogeneities could be explained.

Since Turing's proposal, much theoretical and experimental work has gone into studying these *Turing patterns*. Notably, direct experimental realizations of Turing patterns in controlled chemical systems have been observed [3, 4]. Models featuring stable Turing patterns have been proposed to describe various biological phenomena include animal markings [5, 6], synapse receptor domains [7], protein formation [8],

and population dynamics [9, 10, 11]. Among the wide variety of patterns that can be formed through different reaction mechanisms and parameters, Turing's proposal has expanded to include models with superdiffusion [12], noise [13, 14], growing surfaces [15, 16], and advection [17].

Despite these advances, there remain sizable differences between these simplified theoretical models and real-world systems. A notable dissimilarity is the underlying geometry on which these patterns are analyzed. Due to the geometric dependence of the Laplacian operator, one expects a reaction-diffusion system to similarly have steady-state solutions that are geometry dependent. In most theoretical calculations, the underlying geometry is assumed to be flat, with notable exceptions being studies done on spheres [18] and cylinders [19, 5]. This is in contrast with physical systems, which are often characterized by complex geometries with non-uniform curvature. With regards to these systems, only a handful of numerical studies have been done [20, 8, 21, 22]. The goal of this thesis is to introduce a new class of geometries on which Turing patterns - and by association, the Laplacian operator - can be studied analytically, and to analyze the geometric dependence of these patterns. These geometries can be characterized as small deformations from underlying shapes whose properties are much simpler, as illustrated in Figure 1-1. In addition, we study the behavior of Turing patterns on these geometries, shedding light on the curvature-dependence of patterns resulting from diffusional instabilities.

The importance of non-uniform curvature on collective behavior has been recently studied in liquid crystals [23], flocking [24], and wave propagation [25]. Moreover, geometry has played an important role in studying biological systems at the level of cells [26, 27] and proteins [8], although a direct curvature-sensing mechanism is often assumed - for example, in [8], concentrations are taken to couple directly to the Gaussian curvature. Recently, a model for the protein patterning in *Escherichia coli* was proposed which allows for geometric dependence without an explicit curvature-sensing mechanism [28]. This dependence comes from interactions between membrane-bound proteins and bulk chemicals, since diffusion within the bulk around areas of high curvature lead to more interactions with the membrane. However, the implicit curvature-

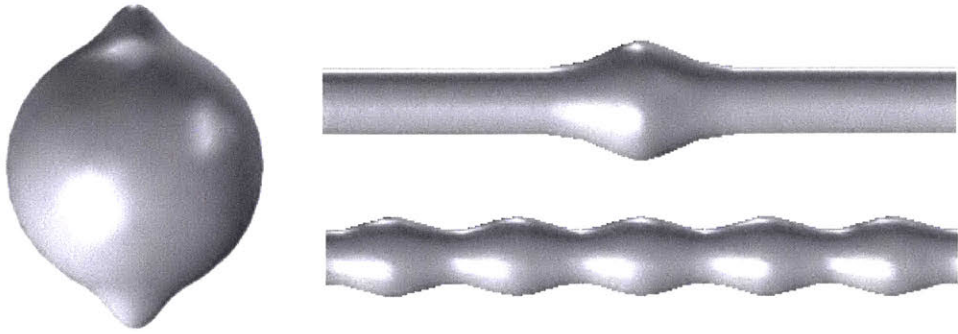


Figure 1-1: A selection of geometries for which Turing patterns can be studied analytically - a cylinder with a radially-symmetric Gaussian bump, a cylinder with a periodic deformation, and a sphere with Gaussian bumps on either pole, respectively.

sensing of biological patterns on surface-bound concentrations remains relatively unexplored. This thesis provides a framework in which one can study this mechanism, which may find applications in a variety of biological systems.

## 1.2 Thesis Structure

In Chapter 2, we begin with a linear stability analysis of the two-component reaction-diffusion equation. In doing so, we gain intuition on exactly where and how geometry plays a role in pattern formation.

Having defined the relevant aspects of a system that geometry can affect - namely, the spectrum of the Laplacian operator - we study in Chapter 3 how they are modified in the class of geometries previously outlined.

In Chapter 4, we examine several noteworthy instances of these geometries - a drum with a Gaussian deformation, a rippled cylinder, a cylinder with a radially symmetric Gaussian bump, and a sphere with an azimuthally symmetric Gaussian bump - and obtain theoretical predictions regarding the behavior of Turing patterns on them. These predictions are compared with numerical simulations done through COMSOL Multiphysics® [29] to verify their validity.

In Chapter 5, we expand our model of Turing patterns to include advection terms, and present preliminary analyses of the resulting time-dependent patterns in the

presence of curvature.

# Chapter 2

## Pattern Formation in Reaction-Diffusion Systems

### 2.1 Linear Stability Analysis of Reaction-Diffusion Systems

In this section, we outline an analysis similar to Turing's original work [2], and demonstrate the ability for a generic reaction-diffusion equation

$$\frac{\partial \mathbf{C}}{\partial t} = \mathbf{D} \Delta \mathbf{C} + \mathbf{R}(\mathbf{C}), \quad (2.1)$$

to admit spatially heterogeneous solutions. Here, we take  $\mathbf{C}$  to be a two-component vector describing the concentrations of two chemicals, and  $\mathbf{D}$  to be a diagonal matrix containing the relative diffusion rates, i.e.

$$\mathbf{C}(\mathbf{r}, t) = \begin{pmatrix} C_1(\mathbf{r}, t) \\ C_2(\mathbf{r}, t) \end{pmatrix} \quad \mathbf{D} = \begin{pmatrix} 1 & 0 \\ 0 & \beta \end{pmatrix}.$$

We proceed by analyzing the stability of homogeneous solutions of Eq 2.1 that are stable in the absence of diffusion. To this end, we linearize the reaction-diffusion equations around this fixed point, and study fluctuations from the homogeneous solution

$\mathbf{C}^*$ .

$$\mathbf{C}(\mathbf{r}, t) \equiv \mathbf{C}^* + \mathbf{c}(\mathbf{r}, t) \quad \Rightarrow \quad \frac{\partial \mathbf{c}}{\partial t} \approx \mathbf{D} \Delta \mathbf{c} + \mathbf{M} \mathbf{c}, \quad (2.2)$$

where

$$M_{ij} = \left. \frac{\partial R_i}{\partial C_j} \right|_{C^*}.$$

If we find that certain inhomogeneous perturbations are unstable - they grow over time as opposed to decaying away - then this indicates the onset of pattern formation. These perturbations are eventually stabilized by non-linear terms in Eq. 2.1, resulting in a steady-state pattern.

To proceed with the analysis, we decompose the spatial dependence of  $\mathbf{c}$  into a sum of Laplacian eigenfunctions, i.e.

$$\mathbf{c}(\mathbf{r}, t) = \sum_k \tilde{\mathbf{c}}_k(\mathbf{r}, t), \quad \Delta \tilde{\mathbf{c}}_k = \lambda_k \tilde{\mathbf{c}}_k. \quad (2.3)$$

Our reaction-diffusion equations then become

$$\frac{\partial \tilde{\mathbf{c}}_k}{\partial t} = (\mathbf{M} + \lambda_k \mathbf{D}) \tilde{\mathbf{c}}_k. \quad (2.4)$$

The  $2 \times 2$  matrix  $\mathbf{M} + \lambda_k \mathbf{D}$  has two eigenvalues which govern the time evolution of its respective mode  $\tilde{\mathbf{c}}_k$ . If either of the eigenvalues is positive, the mode  $\tilde{\mathbf{c}}_k$  is unstable, with the form of the resulting pattern governed by the most unstable  $\tilde{\mathbf{c}}_k$ .

The eigenvalues  $\omega$  of Eq. 2.4 satisfy the equation

$$\begin{aligned} \omega^2 + \omega [-\lambda_k (1 + \beta) - (M_{11} + M_{22})] + h(\lambda_k) &= 0, \\ h(\lambda_k) &= \beta \lambda_k^2 + (M_{11}\beta + M_{22}) \lambda_k + (M_{11}M_{22} - M_{12}M_{21}). \end{aligned} \quad (2.5)$$

The assumption that the homogeneous solution  $\mathbf{C}^*$  is stable implies that  $M_{11} + M_{22} < 0$  and  $M_{11}M_{22} - M_{21}M_{12} > 0$ . Moreover, we assume that  $\lambda_k \leq 0$  - a statement which holds true in all the relevant systems we consider. With these assumptions, positive

values of  $\omega$  are possible only if

$$\beta M_{11} + M_{22} > 0. \quad (2.6)$$

This is the condition that determines whether reaction-diffusion systems have diffusional instabilities. Notably, since  $M_{11} + M_{22} < 0$ , we must have  $\beta \neq 1$  for an instability to form - the two chemicals cannot have identical diffusion rates.

This instability condition also determines the sign of  $M_{11}$  and  $M_{22}$  - if  $\beta > 1$ , then  $M_{11} > 0$  and  $M_{22} < 0$ , and vice versa if  $\beta < 1$ . These diagonal terms in the linearized reaction matrix are associated with excitation (inhibition) for positive (negative) terms. Hence, diffusional instabilities tend to be associated with *long-range inhibition* and *short-range excitation*.

## 2.2 Geometric Dependence of Pattern Formation

The above analysis makes no reference to an underlying geometry. The instability condition, Eq. 2.6, is determined solely through features of the reaction term and relative diffusion rates. Nevertheless, geometry plays an important role in pattern formation. The geometric dependence comes through Eq. 2.3, where we decompose our perturbation as a sum of Laplacian eigenfunctions. The Laplacian operator is intrinsically geometry dependent, and both the form of its eigenfunctions and the spectrum of its eigenvalues can change depending on the underlying geometry. As a result, geometric deformations can have several possible effects on pattern formation, detailed below.

### 2.2.1 Pattern Changes

The form of the Laplacian eigenfunctions vary widely depending on the geometry - plane waves on a flat surface, spherical harmonics on the surface of a sphere, et cetera. As these eigenfunctions drive the onset of pattern formation, one would expect the variation in these eigenfunction solutions to be made manifest in the form

of the resulting patterns. This is true, but only insomuch as the eigenfunctions can be indicative of the exact form of the resulting pattern. In many actual models of reaction-diffusion systems, features of the non-linear reaction terms are often the primary indicator of the resulting patterns. Nevertheless, the form of the Laplacian eigenfunctions can substantially effect the form of the resulting patterns in some systems, which gives a clear method for geometry to affect patterning.

More subtle pattern changes can also arise due to geometry changes. For example, it was noted in [18] that perfectly striped Turing patterns on spheres cannot arise due to the hairy ball theorem.

### 2.2.2 Symmetry Breaking

Symmetries in a geometry can be reflected by degeneracies in the Laplacian spectrum. Translational symmetry on a line leads to a two-fold degeneracy in the Laplacian spectrum - sine and cosine modes with the same frequency - which further implies translational symmetry in the eigenfunctions. Similarly, rotational symmetry in the surface of a sphere results in the  $2\ell+1$  fold degeneracy in the spherical harmonics  $Y_\ell^m$ , which allows generation of rotational symmetry through Wigner d-matrices [30]. The patterns that form exhibit similar symmetries. If one considers a geometry with some symmetry, and then deforms the geometry in a manner that breaks the symmetry, one expects the respective Laplacian degeneracy to be broken, leading to a “pinning” of the patterns that form. This phenomenon is explored more thoroughly in Chapter 4. This effect is noteworthy because, unlike the method described in Section 2.2.1, geometric consequences can present themselves through only small changes to the geometry.

### 2.2.3 Instability through Spectrum Shifts

The linear analysis of reaction-diffusion systems indicate that, given certain geometry-independent facts, there exist a set of Laplacian eigenvalues whose corresponding eigenmodes are unstable. However, a combination of geometric facts and boundary

conditions can discretize the Laplacian spectrum and only admit certain modes. For example, a flat square plane with length  $L$  and Dirichlet boundary conditions only admits eigenvalues that satisfy  $\lambda_{nm} = -(n\pi/L)^2 - (m\pi/L)^2$  for some integers  $m$  and  $n$ . If the set of unstable eigenmodes does not satisfy these conditions, the homogeneous solution will be stable and no pattern will be formed. Through a combination of area changes and curvature effects, geometric deformations will generically modify the spectrum of the Laplacian, which can in turn permit previously excluded eigenmodes to grow and develop into patterning. Similar to the symmetry breaking phenomenon, this effect can become manifest through small changes to an underlying geometry, although one would not expect this to be generic with respect to the parameters of the reaction-diffusion equation - the coefficients would need to be tuned such that the band of unstable eigenmodes is smaller than the gap in allowed eigenvalues.

#### 2.2.4 Non-Linear Effects

Although not derivable purely on the basis of the linear analysis, one may plausibly hypothesize that non-linear effects outside the regime of small perturbations would lead to unique geometric dependencies of pattern formation. Recently, a numerical study of Turing patterns on spine-like geometries found evidence of concentration localization to areas of high curvature [22]. These effects, while inaccessible analytically, may be explored numerically.



# Chapter 3

## Laplacian Modifications From Geometric Perturbations

### 3.1 Developing a Perturbation Theory via Conformal Mapping

As previously detailed, small geometric changes can have noticeable consequences in the resulting Turing patterns. In this section, we develop a generic method of studying Laplacian modifications due to these changes.

We begin by considering the geometry that we wish to study - a rippled cylinder, a sphere with a bump, et cetera. This geometry possesses a metric  $G_{ij}$  and coordinates  $(x, y)$ , through which the Laplacian is defined as [31]

$$\Delta^G \phi = \frac{1}{\sqrt{G}} \partial_i \left( \sqrt{G} G^{ij} \partial_j \phi \right), \quad (3.1)$$

where we define  $G \equiv \det(G_{ij})$  and  $G^{ij} \equiv G_{ij}^{-1}$ . For a generically deformed surface, Eq 3.1 will not yield closed-form solutions, and is difficult to study on its own. To make progress, we now introduce a reparameterization of the metric  $(x, y) \rightarrow (u, v)$  with respect to a simpler geometry,  $g_{ij}$

$$G_{ij} \equiv \Omega^2(u, v) g_{ij}. \quad (3.2)$$



Figure 3-1: A conformal mapping from a complex geometry - a hand - to a sphere. The uniform mesh on the hand is now pinched at certain areas on the sphere, preserving information regarding the structure of the fingers. [1]

$\Omega$  is known as the conformal factor. Reparameterizations of the form Eq 3.2 are called *conformal mappings*. Intuitively, one can interpret this process as taking a complex surface and mapping it to a simpler geometry, but preserving intrinsic features such as distance, see Fig. 3.1.

Conformal mappings have many applications ranging from fluid mechanics [32] to electrodynamics [33], as the simple form of Eq. 3.2 leads to the relation

$$\Delta^G = \frac{1}{\Omega^2} \Delta^g. \quad (3.3)$$

If  $G_{ij} = g_{ij}$ , then clearly  $\Omega^2 = 1$ . However, if  $G_{ij}$  and  $g_{ij}$  differ by some small bookkeeping parameter  $\epsilon$ , then it would be reasonable to expect that  $\Omega^2 = 1 + \mathcal{O}(\epsilon)$ . This suggests that we may be able to treat Eq. 3.3 perturbatively, taking the eigenfunctions of  $\Delta^G$  to satisfy  $[\Delta^g + \mathcal{O}(\epsilon)] \phi = \lambda \phi$  in the conformal coordinates  $(u, v)$ , and then calculating eigenfunction/value corrections from this equation. Below, we provide explicit derivations of this form for general perturbations to a class of base geometries.

### 3.1.1 Perturbations of a Flat Planar Drum

As a first example, we consider the surface of a flat planar drum with coordinates  $(r, \varphi)$  and a circularly symmetric bump characterized by a height function  $h(r)$ . The

line element on this surface is given by

$$ds^2 = g_{ab} dx^a dx^b = (1 + h_r^2) dr^2 + r^2 d\varphi^2 . \quad (3.4)$$

We now define a conformal mapping to a flat planar drum. The symmetry of the bump implies that the conformal mapping defined by Eq. 3.2 only modifies the radial component, i.e.  $(r, \varphi) \rightarrow (u, \varphi)$ . This symmetry is crucial to the tractability of the following calculations. We obtain this conformal mapping by setting the line elements to be equal,

$$ds^2 = (1 + h_r^2) dr^2 + r^2 d\varphi^2 = \Omega^2(u) (du^2 + u^2 d\varphi^2) . \quad (3.5)$$

From this, we can calculate both the conformal factor  $\Omega(u)$ , as well as the relation between the physical coordinate  $r$  and the conformal coordinate  $u$ . By equating the radial and angular components of Eq. 3.5 separately, we obtain the constraints

$$\begin{aligned} (1 + h_r^2) dr^2 &= \Omega^2(u) du^2 , \\ r^2 &= \Omega^2(u) u^2 . \end{aligned}$$

Eliminating  $\Omega$ , it follows that

$$(1 + h_r^2) = \frac{r^2}{u^2} \left( \frac{du}{dr} \right)^2 ,$$

from which the general form of  $u(r)$  is

$$u = Cr \exp \int_0^r \left[ (1 + h_r^2)^{\frac{1}{2}} - 1 \right] \frac{dr}{r} , \quad (3.6)$$

for some integration constant  $C$ . Fixing  $u(0) = 0$  sets  $C = 1$ .

We now take the gradients of  $h$  to be small,  $|h_r| \ll 1$ , so that Eq. 3.6 can be treated perturbatively. It should be noted that this assumption is separate from taking our deformation to be small,  $|h(r)| \ll 1$ . While relevant to many cases of interest, this perturbation theory is not applicable to, say, Gaussian bumps with

$\sigma \ll 1$ , or a rippled deformation with wave vector  $k \gg 1$ .

To second order in  $h_r$ , Eq. 3.6 can be inverted to obtain

$$r \approx u \left( 1 - \frac{1}{2} \int_0^u \frac{du}{u} h_u^2 \right). \quad (3.7)$$

With this,  $\Omega$  can be expressed purely in terms of  $u$  as

$$\Omega^2 = \left( 1 - \frac{1}{2} \int_0^u \frac{du}{u} h_u^2 \right)^2. \quad (3.8)$$

As expected, our expression for  $\Omega$  is equal to 1 plus terms that can be treated perturbatively under certain conditions.

With the corresponding flat Laplacian in mind, we define our eigenvalues as  $-k^2$ , such that eigenfunctions  $\phi_k$  satisfy

$$\Delta^g \phi_k = -k^2 \phi_k.$$

Writing our expression in conformal coordinates, our equation becomes

$$-\Delta^0 \phi_k = k^2 \Omega^2(u) \phi_k. \quad (3.9)$$

Using the approximation from Eq. 3.8, this equation becomes

$$[-\Delta^0 + V(u)] \phi_k = k^2 \phi_k, \quad (3.10)$$

where

$$V(u) = k^2 \int_0^u du \frac{h_u^2}{u}.$$

With this, the choice defining our eigenvalues as  $-k^2$  becomes evident. Our eigenvalue equation becomes identical to the Schrödinger equation of a quantum mechanical particle in a potential  $V(u)$ . This equation is tractable though a slight modification to standard Rayleigh-Schrödinger perturbation theory - outlined in Appendix A - and can be used to calculate geometric modifications to Laplacian eigenfunctions and

eigenvalues.

While the above result provides the conceptual foundation for our approach, the exact form turns out to be cumbersome when doing actual calculations. To simplify this slightly, we can redefine the limits of integration and obtain

$$[-\Delta^0 + V(u)] \phi_k = k^2 (1 - \Gamma) \phi_k , \quad (3.11)$$

where we now define

$$V(u) = -k^2 \int_u^\infty du \frac{h_u^2}{u} ,$$

and

$$\Gamma = \int_0^\infty du \frac{h_u^2}{u} .$$

### 3.1.2 Perturbations from a Uniform Cylinder

The second example we consider is a cylinder with radius  $R_0$ . Using cylindrical polar coordinates, radially-symmetric deformations from this geometry can be described by a position-dependent radius,  $R(z) = R_0(1 + h(z))$ . The line element on this surface is given by

$$ds^2 = (1 + R_0^2 h_z^2) dz^2 + R_0^2 (1 + h)^2 d\varphi^2 . \quad (3.12)$$

Following the procedure in the previous section, we map this to a conformally flat cylinder, whose line element is given by

$$ds^2 = \Omega^2(v) (dv^2 + R_0^2 d\varphi^2) . \quad (3.13)$$

The equality between the two line elements implies the relationship

$$v = \int_0^z (1 + R_0^2 h_z^2)^{\frac{1}{2}} \frac{dz}{1 + h(z)} + C . \quad (3.14)$$

The condition  $v \sim z$  at  $z = 0$  implies that  $C = 0$ . To first order in  $h$  and its gradients,

$$v \approx z - \int_0^z h(z) dz . \quad (3.15)$$

The conformal factor is given by Eq. 3.12 and 3.13 as

$$\Omega^2 = (1 + h(v))^2 . \quad (3.16)$$

Unlike the case of a planar drum, the conformal factor does not explicitly depend on the relationship between the conformal and physical coordinates. However, the derivation of Eq. 3.15 is still necessary, as the height function  $h(z)$  must be re-expressed in the conformal coordinates as  $h(v)$ .

To first order in  $h$  and its gradients, Laplacian eigenfunctions  $\phi_k$  with eigenvalue  $-k^2$  satisfy the equation in conformal coordinates

$$[-\Delta^0 - 2k^2 h(v)] \phi_k = k^2 \phi_k . \quad (3.17)$$

In this case, the quantum mechanical intuition behind geometric Laplacian modifications is even stronger. In the conformally flat coordinates, the geometric deformations are manifest as a potential whose qualitative features directly mirror those of the deformation itself. This observation suggests several results - for example, a periodic deformation, such as a rippled cylinder, would lead to a band gap near the periodicity of the deformation, in the same way that the periodic potential in a 1D crystal leads to a bandgap in the electron energy spectrum. This hypothesis will be examined further in Chapter 4.

A noteworthy difference between Laplacian corrections on cylinders and planar drums is the difference in orders - the former has first order corrections, while the latter only has correction terms of second order and higher. The intuition behind this is geometric - linear correction terms differentiate between positive and negative height functions, or outward and inward deformations. In the case of a cylinder, an inward bump is different than an outward bump; however, on a planar drum, the two are equivalent. This is further reflected in the form of our eigenvalue corrections - the sign of the potential in Eq. 3.17, and hence the sign of the first-order eigenvalue corrections, switches depending on whether the deformation is inward or outward.

### 3.1.3 Perturbations from a Uniform Sphere

As a final example, we develop a framework for analyzing axially symmetric deformations of a uniform sphere. Working in spherical coordinates, these surfaces can be described by an angular-dependent radius,  $R(\theta) = R_0(1 + h(\theta))$ . In these coordinates, the line element is given by

$$ds^2 = ((1 + h(\theta))^2 + h_\theta^2) R_0^2 d\theta^2 + R_0^2 (1 + h(\theta))^2 \sin^2 \theta d\varphi^2 . \quad (3.18)$$

We map this to a conformally-flat sphere,

$$ds^2 = \Omega^2 (d\Theta^2 + \sin^2 \Theta d\varphi^2) . \quad (3.19)$$

With this, we obtain the ODE relating  $\Theta$  and  $\theta$

$$\sin^2 \theta \Theta'^2 = \sin^2 \Theta \left( 1 + \frac{R'^2}{R^2} \right) . \quad (3.20)$$

This equation can be analyzed perturbatively, and to first order in  $h$ ,  $\Theta = \theta$ . Using Eq. 3.18 and 3.19 to solve for  $\Omega$ , we find that eigenvalues and eigenfunctions satisfy

$$[-\Delta^0 - 2k^2 R_0^2 h] \phi_k = k^2 R_0^2 \phi_k . \quad (3.21)$$

The additional term on the LHS of Eq. 3.21 breaks the polar symmetry in the eigenfunctions, effectively “fixing” the resulting polar orientation of the eigenfunctions (although azimuthal symmetry is preserved).

Eigenvalue corrections to the spherical harmonic eigenfunctions  $Y_{\ell m}$  can be calculated via perturbation theory from Eq. 3.21 to obtain

$$\lambda_{\ell m} = \lambda_{\ell m}^{(0)} - 2\epsilon \lambda_{\ell m}^{(0)} \int_0^\pi d\theta \int_0^{2\pi} d\phi Y_{\ell m}^*(\theta, \phi) h(\theta) Y_{\ell m}(\theta, \phi) + \mathcal{O}(\epsilon^2) . \quad (3.22)$$

From this, one can obtain several qualitative results. An immediate result is that, similar to the case of a deformed cylinder, the eigenvalue corrections are sensitive to

the sign of  $\epsilon$  - an inward deformation gives the opposite eigenvalue correction as an outward deformation. Furthermore, if  $h(\theta) = h(-\theta)$ , then we have

$$\begin{aligned} \int_0^\pi d\theta \int_0^{2\pi} d\phi Y_{\ell m}^*(\theta, \phi) h(\theta) Y_{\ell m}(\theta, \phi) &= \int_{-\pi}^0 d\theta \int_0^{2\pi} d\phi Y_{\ell m}^*(\theta, \phi) h(\theta) Y_{\ell m}(\theta, \phi) \\ &= \int_0^\pi d\theta \int_0^{2\pi} d\phi Y_{\ell m}^*(\theta, \phi) h(\theta + \pi) Y_{\ell m}(\theta, \phi). \end{aligned}$$

where we have used the relations  $Y_{\ell m}(\theta, \phi) = \pm Y_{\ell m}(\theta + \pi, \phi) = \pm Y_{\ell m}(-\theta, \phi)$ . This implies that two deformations at either pole give first order eigenvalue corrections twice as large as a single deformation, provided the height function is symmetric.

A final observation is that first-order eigenvalue corrections vanish when  $h(\theta + \pi/2) = -h(\theta - \pi/2)$ , or when  $h$  is odd. The intuition behind this is similar to the vanishing of first-order corrections on a drum - since inverting the sign of the height function would lead to qualitatively the same deformation, eigenvalue corrections ought to only be dependent on even powers of  $h$ . Unusually, first order eigenfunction corrections are generally non-vanishing in these cases.

# Chapter 4

## Geometric Modifications of Turing Patterns

Having developed a method for perturbatively calculating Laplacian eigenfunction and eigenvalue modifications, we study several specific geometries, focusing on eigenvalue modifications and their implications for Turing pattern development.

### 4.1 Gaussian Deformations of a Drum

#### 4.1.1 Eigenvalue Modifications

As a first application, we consider perturbations of a flat drum with radius  $R_0$  with Dirichlet boundary conditions imposed on the edge. In the absence of a deformation, Laplacian eigenfunctions are given by

$$\phi_{mn}^{(0)}(r, \theta) = J_m\left(\frac{x_{mn}r}{R}\right) e^{\pm im\theta},$$

where  $J_m(x)$  is the  $m$ -th order Bessel function of the first kind, and  $x_{mn}$  is the  $n$ -th zero of  $J_m(x)$  (if Neumann boundary conditions were imposed, one would instead use the zeros of the derivative of the Bessel function). The eigenvalues are given by

$$\lambda_{mn}^{(0)} = -\left(\frac{x_{mn}}{R}\right)^2.$$

As Bessel functions are traditionally unnormalized, one must implicitly include a normalization constant so that an orthonormal basis is used.

We now consider a Gaussian deformation to the cylinder,

$$h(r) = v_0 \exp\left[-\frac{r^2}{2\sigma^2}\right].$$

In the conformally flat coordinates, the radius of the drum is stretched - Eq. 3.6 gives the relation between the actual radius  $R_0$  and the conformal radius  $R$  by

$$R = R_0 \left(1 + \frac{1}{2} \int_0^{R_0} \frac{dr}{r} h_r^2\right) \equiv R_0 + R'. \quad (4.1)$$

This increase in length changes the discretization of the allowed eigenfunctions, and in turn, the allowed eigenvalues. Complete corrections are obtained by this term combined with eigenvalue corrections given by Rayleigh-Schrödinger perturbation applied to Eq. 3.11, where our “potential” is given to second order in the gradient by

$$V(u) = -\lambda_{mn}^{(0)} \int_u^\infty \frac{du}{u} h_u^2 = -\frac{\lambda_{mn}^{(0)} v_0^2}{2\sigma^2} e^{-\frac{u^2}{\sigma^2}}.$$

Although analytic solutions to these lowest-order corrections do not exist, the results can easily be plotted numerically, as shown in Fig. 4-1. From this, one can extract several results. Firstly, the size of these corrections decay quickly as  $\sigma$  grows, in agreement with the fact that an increasing  $\sigma$  corresponds to a smaller gradient. Likewise, corrections grow as  $\sigma$  approaches zero, and perturbation theory breaks down as the gradient diverges. Additionally, as our corrections are proportional to  $\lambda_{mn}^{(0)}$ , the size of the correction scales approximately linearly with the size of  $\lambda_{mn}^{(0)}$  (nonlinear scaling is introduced through the Rayleigh-Schrödinger perturbation theory, where the correction is also dependent on the form of  $\phi_{mn}^{(0)}$ ).

### 4.1.2 Turing Pattern Modifications

Although the deformation under consideration does not break any symmetries, which would suggest the possibility of the pinning of Turing patterns, the eigenvalue shift

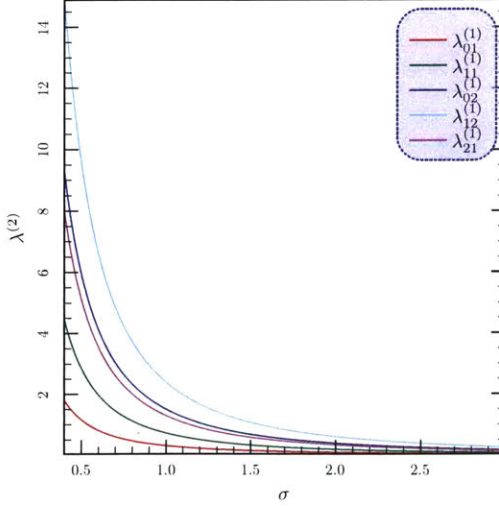


Figure 4-1: Second-order eigenvalue corrections to Laplacian eigenfunctions on a drum with a Gaussian deformation, plotted as a function of  $\sigma$ , for  $R_0 = 5$  and  $v_0 = 0.5$ . The plot illustrates the vanishing of eigenvalue corrections as  $\sigma \rightarrow \infty$ .

induced by the perturbation provides a simple example of geometric deformations destabilizing eigenfunctions that had previously been stable. Additionally, since different Bessel functions have qualitatively different shapes, this eigenvalue shift could cause the most unstable mode to switch from one eigenmode to another, thereby changing the nature of the resulting patterns. However, these conclusions are made within the linear analysis carried out in Chapter 2, which merely describes the onset of stability. To determine whether this instability-inducing effect is present in the fully-developed Turing pattern, we conduct finite element simulations of the Thomas-Murray model [5]:

$$\begin{aligned} \frac{\partial C_1}{\partial t} &= \nu_1 \Delta^G C_1 + \gamma \left( u_{10} - C_1 - \frac{\rho C_1 C_2}{1 + C_1 + C_1^2/K} \right) \\ \frac{\partial C_2}{\partial t} &= \nu_2 \Delta^G C_2 + \gamma \left( \alpha (u_{20} - C_2) - \frac{\rho C_1 C_2}{1 + C_1 + C_1^2/K} \right) . \end{aligned}$$

These simulations were carried out using COMSOL Multiphysics®, which approximates the Laplacian by finite differences on a mesh. The results of these simulations are displayed in Fig. 4-2, which shows that a reaction-diffusion system stable in the absence of a bump can be made unstable and form inhomogeneous patterning in

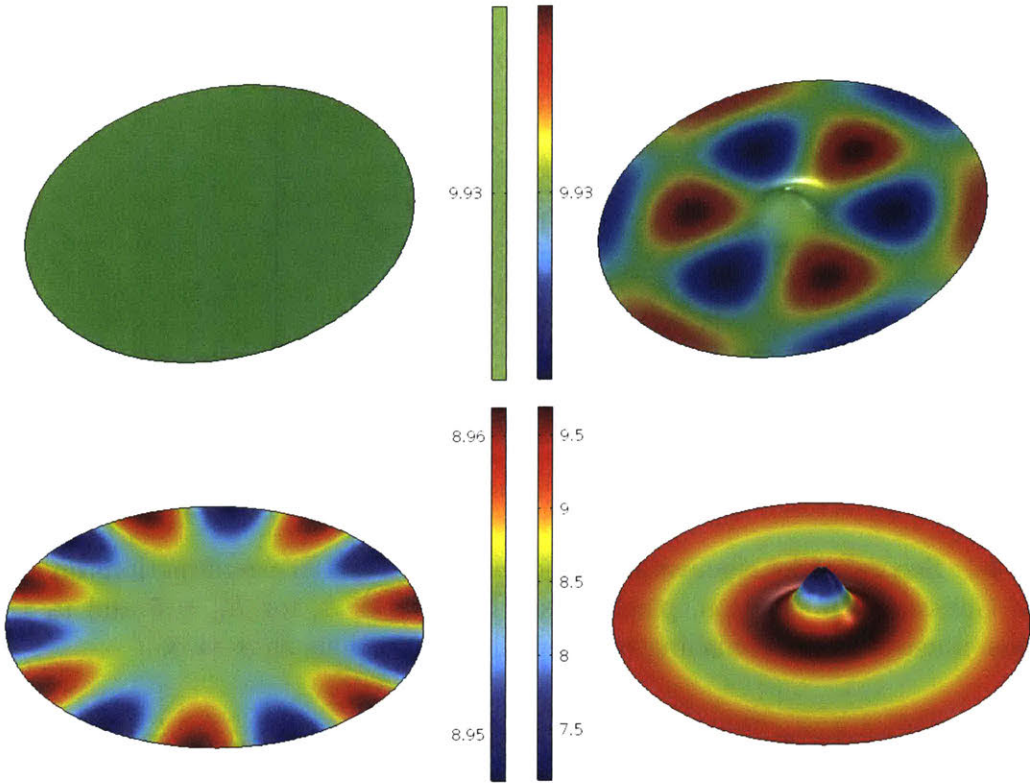


Figure 4-2: (Top) An undeformed drum, whose Laplacian eigenfunctions are stable. However, a Gaussian deformation modifies the Laplacian eigenfunctions, permitting unstable modes and allowing an inhomogenous pattern to grow. (Bottom) In addition to modifying the stability of eigenfunctions, geometric perturbations can change which eigenfunctions are most unstable, thereby modifying the resulting patterns.

the presence of a bump. Moreover, the type of pattern can be modified by the deformation, corresponding to the qualitatively different forms of the different Bessel functions.

## 4.2 Gaussian Deformations of a Cylinder

### 4.2.1 Eigenvalue Modifications

We now switch focus to perturbations of a uniform cylinder of length  $L$  and radius  $R_0$ . We impose periodic boundary conditions on the cylinder; hence, the unperturbed

eigenfunctions and eigenvalues are given by

$$\begin{aligned}\phi_{sk}^{(0)} &= \frac{e^{is\varphi}}{\sqrt{2\pi R_0}} \frac{e^{i2\pi kz/L}}{\sqrt{L}}, \\ \lambda_{sk}^{(0)} &= -\frac{s^2}{R_0^2} - \left(\frac{2\pi k}{L}\right)^2 \equiv -\bar{s}^2 - \bar{k}^2,\end{aligned}\tag{4.2}$$

with integers  $s$  and  $k$ .

We now consider a radially-symmetric Gaussian bump, described by the height function

$$h(z) = \epsilon \exp\left[-\frac{z^2}{2\sigma^2}\right].\tag{4.3}$$

To first order in  $\epsilon$  and  $R_0 h_z$ , the height function  $h$  is the same in both the initial and conformal coordinates. In the conformally-flat coordinates, the length of the cylinder is modified, and the allowed values of  $\bar{k}$  are modified to first order in  $\epsilon$  as

$$\bar{k}' = \bar{k} \left(1 + \frac{\epsilon\sigma\sqrt{2\pi}}{L}\right),\tag{4.4}$$

to satisfy the prescribed boundary conditions.

Corrections to these eigenfunctions can be calculated perturbatively in  $\epsilon$  using Eq. 3.17, which to first order reads

$$\left[-\frac{\partial^2}{\partial v^2} + \bar{s}^2 - 2\epsilon\lambda_{sk}^{(0)} e^{-\frac{v^2}{2\sigma^2}}\right] Z_{sk}(v) = \lambda_{sk} Z_{sk}(v),\tag{4.5}$$

with  $\phi_{sk} \equiv Z_{sk}(v)e^{is\varphi}/\sqrt{2\pi R_0}$ . Note the sign of our potential: an attractive (repulsive) potential corresponds to an outward (inward) bump. We now apply Rayleigh-Schrödinger perturbation theory to calculate first order eigenvalue corrections, which simplify in the case of  $s = 0$  to

$$\begin{aligned}\lambda_{sk} &= -\bar{s}^2 - \bar{k}^2 - \overbrace{\frac{2\epsilon\bar{k}^2\sigma\sqrt{2\pi}}{L}}^{\text{Eq. 4.4}} + \overbrace{\frac{2\epsilon\sigma\bar{k}^2\sqrt{2\pi}}{L} \left(1 \pm e^{-2\bar{k}^2\sigma^2}\right)}^{\text{Effective Potential}} \\ &= \lambda_{sk}^{(0)} \pm \frac{2\epsilon\sigma\sqrt{2\pi}}{L} e^{-2\bar{k}^2\sigma^2}.\end{aligned}\tag{4.6}$$

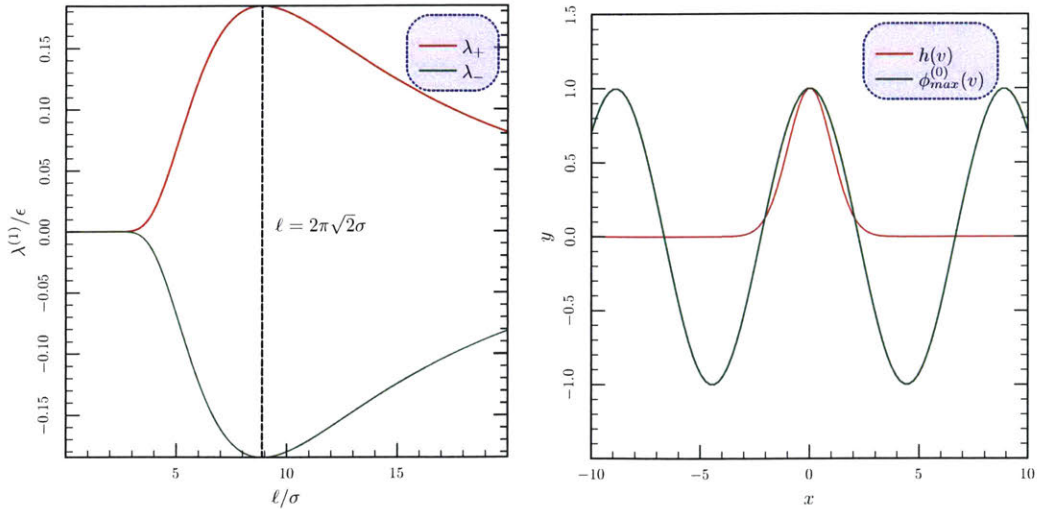


Figure 4-3: (Left) The first-order eigenvalue corrections for the symmetric and anti-symmetric modes, plotted as a function of wavelength  $\ell$  relative to the standard deviation of the Gaussian bump  $\sigma$ . (Right) The eigenfunction that receives the largest first-order correction compared with the width of the Gaussian bump. The wavelength of this eigenfunction is approximately twice the width of the bump.

The positive/negative sign is determined by the mode– cosine (symmetric) modes obtain a positive correction, whereas sine (antisymmetric) modes receive a negative correction. The sign of  $\epsilon$  depends on the orientation of the Gaussian deformation– positive for a bulge and negative for a constriction. Thus, to first order, a Gaussian bump breaks the degeneracy in the eigenvalues of a Laplacian on the cylinder, causing the eigenvalues of sine (cosine) modes to become more negative in the case of an outward (inward) bump. This correction is largest for  $2\pi/\bar{k} = 4\pi\sigma$ , or when the wavelength is approximately twice the width of the bump, as illustrated in Fig. 4-3. This feature is a more general trait of deformations, explored later for a rippled cylinder. Of course, the bump can be positioned at any point along the cylinder, with corresponding shifts of cosine and sine modes to be centered on the Gaussian.

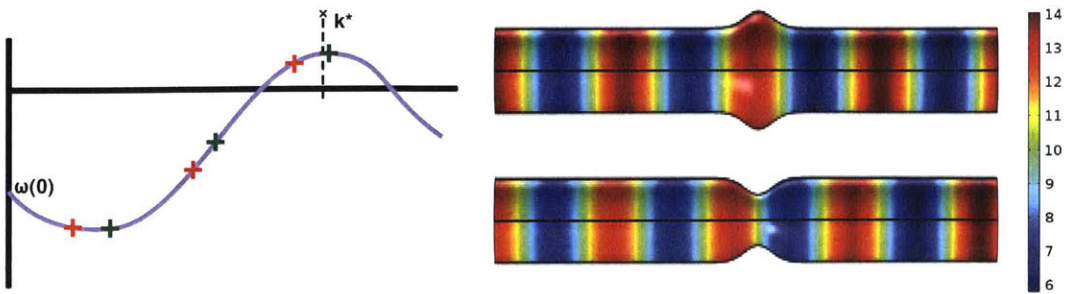


Figure 4-4: (Left) The degeneracy of the allowed eigenmodes on a cylinder is broken by the Gaussian bump, splitting into symmetric and antisymmetric modes, labeled by green and red points. In the context of Turing patterns, one of these modes is closest to the most unstable mode,  $k^*$ , and hence dominates the resulting pattern. (Right) Patterns from the Thomas-Murray reaction-diffusion model in Eq.4.2 are entrained to a Gaussian bump, switching in phase between inward and outward deformations.

#### 4.2.2 Turing Pattern Modifications

##### Comparison of Analytic and Numerical Results

On a uniform cylinder with periodic boundary conditions, Turing patterns exhibit translational symmetry as a result of the degeneracy between sine and cosine eigenfunctions. As shown in Fig. 4-3, this degeneracy is broken by a Gaussian bump, with eigenfunctions becoming “pinned” to the location of the deformation. By the linear analysis of reaction-diffusion systems, this implies that Turing patterns become similarly pinned to the Gaussian bump. To determine whether this feature is present in the fully-developed model with nonlinearities, we again carry out simulations using COMSOL Multiphysics®. The resulting patterns in the presence of the Gaussian bump are shown in Fig. 4-4. The patterns shown illustrate both the pinning of the pattern to the Gaussian bump, as well as the sensitivity of the pinning to the curvature - since the sign of the eigenvalue correction switches between an inward and outward bump, the most unstable mode switches from symmetric to antisymmetric upon inverting the bump.

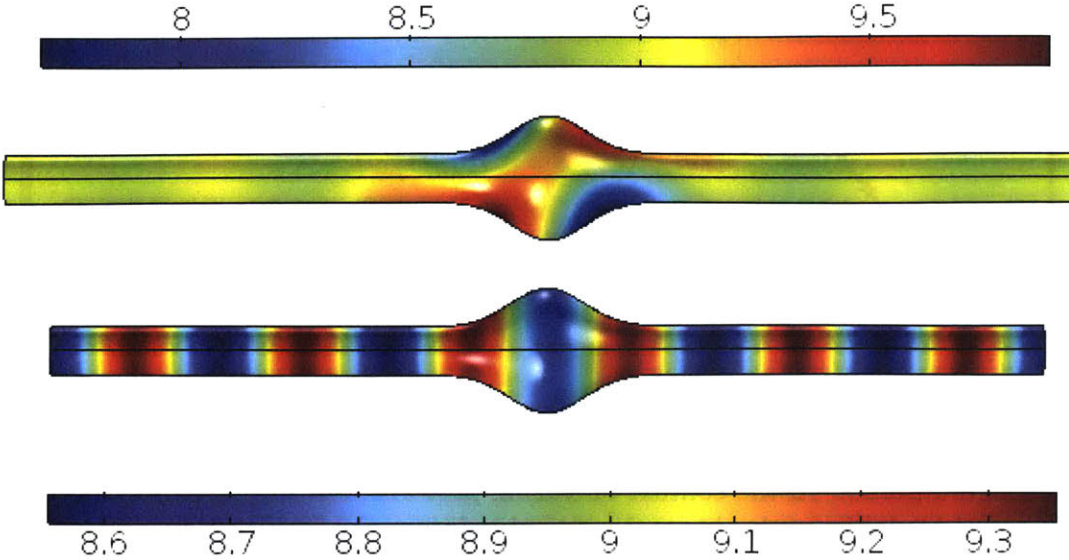


Figure 4-5: Near critical reaction-diffusion equations on geometries with large deformations can lead to localization of the resulting Turing patterns (top), although this phenomenon is sensitive to boundary effects and length scales (bottom).

### Turing Pattern Behavior in the Non-Perturbative Regime

With COMSOL's software, we have the freedom to explore a wide variety geometries, even if they are not accessible by analytical methods. Specifically, one can adjust the height of the Gaussian deformation past the point where perturbation theory becomes a reasonable approximation. With this, one finds surprising behavior as a result of the high curvature. If the reaction-diffusion equation is tuned to be at the threshold of criticality - i.e., only a small band of unstable wavelengths exist - then one finds that a large Gaussian deformation at the center of a cylinder can localize patterns to the bump, as shown in Fig. 4-5, although this localization is dependent on the overall length of the cylinder. This phenomenon is similar to patterning observed in [22], where a numerical study found that higher concentrations of substances in a reaction-diffusion equation on a spine-like geometry are observed on protrusions in the geometry, providing a possible explanation for the localization of GTPase signaling in neurons.

Although the Laplacian modifications due to such a large deformation are unobtainable given the conformal mapping approach, one may still hypothesize the mech-

anisms that cause such a localization. A potential theory is given by the following stages. An initial instability causes a globally unstable mode to grow exponentially, covering both the deformed region of the cylinder and the flat regions. Once non-linearities set in, the portion on the cylinder will form a localized density, which will act as a new boundary condition for the flat regions. If no unstable modes commensurate with the length of the flat regions and the new boundary conditions exist, the concentrations in the flat regions decay to either a homogeneous solution or a low-amplitude periodic solution corresponding to the  $\omega(k^*) = 0$  mode in the linear analysis. This theory agrees with numerical simulations in that it requires both the reaction-diffusion system to be tuned to near-criticality, and that it predicts the localization phenomena to be dependent on the length of the cylinder (which determine the allowed modes in the flat region). In fact, one observes numerically that the pattern localization vanishes when the length of the cylinder is orders of magnitude longer than the wavelength of the pattern - again in agreement with the proposed mechanism. A longer cylinder corresponds to smaller “gaps” between allowed eigenvalues, and the ability for the system to suppress unstable modes by forbidding them via boundary conditions becomes more difficult as the size of the system grows.

## 4.3 Periodically Rippled Cylinder

### 4.3.1 Eigenvalue Modifications

Again considering a cylinder with periodic boundary conditions, we now introduce a periodic deformation, described by the height function  $h(z) = \cos[(2\pi p/L)z] \equiv \cos(\bar{p}z)$ . This gives the Schrödinger-like equation to  $\mathcal{O}(\epsilon)$

$$\left[ -\frac{\partial^2}{\partial v^2} + \bar{s}^2 - 2\epsilon\lambda_{sk}^{(0)} \cos(\bar{p}v) \right] Z_{sk} = \lambda_{sk} Z_{sk}(v).$$

Analysis of these periodic potentials are well-understood in the context of a one-dimensional crystal [34], and such an analysis can be applied to this scenario as well. The periodicity of our potential causes first-order corrections to vanish except for at

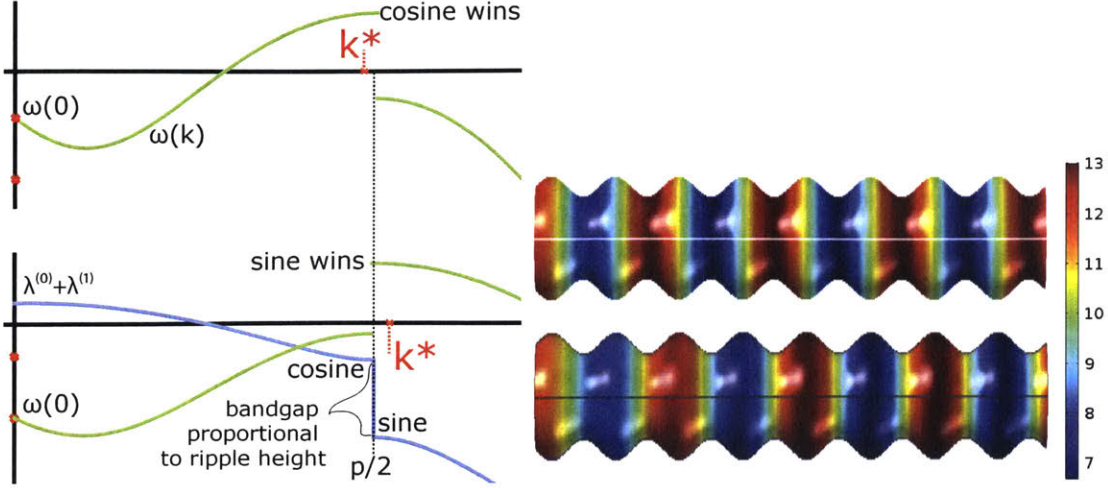


Figure 4-6: (Left) Periodic rippling creates a band gap in the Laplacian spectrum (blue), which in turn creates a similar gap in the Turing dispersion relation (green). This leads to the most unstable mode switching sharply between cosine and sine as the mode is dialed past  $p/2$ . (Right) Numerical simulations of the Thomas-Murray model in COMSOL Multiphysics®, where concentrations switch from troughs to ridges as the most unstable mode passes  $p/2$ .

$k = \pm p/2$ . At this point, degenerate perturbation theory yields a splitting in the eigenvalues, with a magnitude of  $4\epsilon\lambda_{sk}^{(0)}$ .

### 4.3.2 Turing Pattern Modifications

As shown in Fig. 4-6, the periodic rippled cylinder opens a bandgap in the Laplacian spectrum, which in turn leads to a step in the Turing spectrum. As a result of this, one anticipates the most unstable mode  $k^*$  to sharply switch from sine (antisymmetric) to cosine (symmetric) as  $k^*$  is dialed past  $p/2$ . This result is confirmed numerically, as demonstrated in Fig. 4-6.

## 4.4 Gaussian Deformations of a Sphere

### 4.4.1 Eigenvalue Modifications

As a final case, we consider a sphere with two Gaussian bumps on each pole, described by the height functions

$$h(\theta) = \epsilon \exp\left[-\frac{\theta^2}{2\sigma^2}\right] + \epsilon \exp\left[-\frac{(\theta - \pi)^2}{2\sigma^2}\right].$$

Eigenvalue corrections from this deformation are given by Eq. 3.22. While the complexity of spherical harmonics prevents one from deriving analytic results as a function of  $\ell$ , one can numerically plot the first-order eigenvalue corrections to analyze its dependencies. As shown in Fig. 4.4.1, the corrections that we obtain are qualitatively different than with a Gaussian bump on a cylinder (Fig. 4-3). Specifically, the magnitude of the eigenvalue corrections grow quickly, and in fact diverge, with the degree of the spherical harmonic. This is unsurprising given the conformal analysis, as the strength of our “potential” is proportional to  $\lambda_{\ell m}^{(0)}$  - such growth would be present in the analysis of a cylinder as well, had the additional constraint of imposing boundary conditions not canceled this divergence. The correction also increases monotonically with the width of the Gaussian deformation.

### 4.4.2 Turing Pattern Modifications

The deformations described have the effect of breaking the polar symmetry in the Laplacian eigenfunctions, pinning them to the location of the deformation. Simulations of the full reaction-diffusion equation are carried out to determine if this persists in the final Turing patterns. In the simulations, we see the ability for deformations to fix the orientation of the patterns, although incommensurability of length scales and non-linearities can compete against it, see Fig. 4-8. We also note that, similar to the deformed cylinder, eigenfunction modifications are sensitive to the sign of  $h$  - an inward bump causes an increase in diffusion, whereas an outward bump results in the opposite. Although non-linear effects in the Thomas-Murray model on the

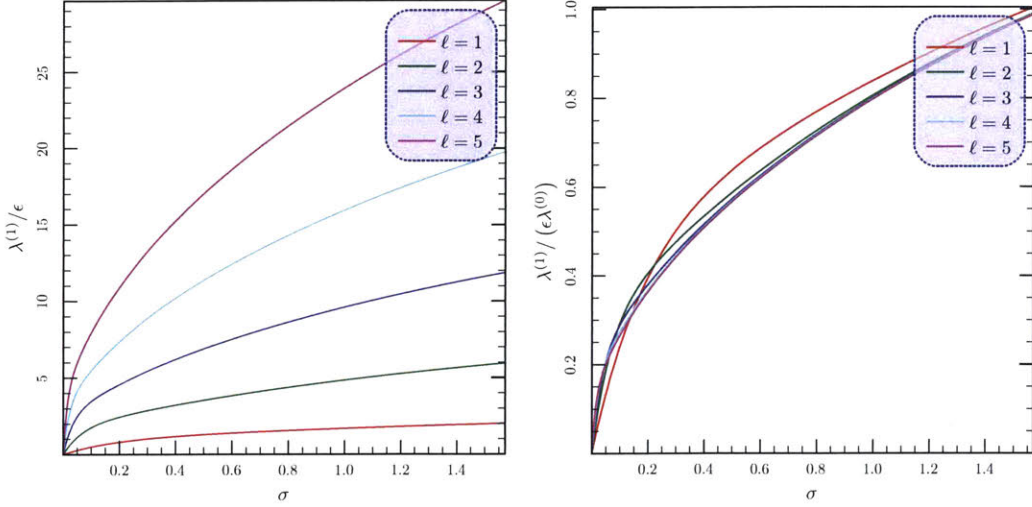


Figure 4-7: (Left) First-order Laplacian eigenvalue corrections from two Gaussian deformations on either pole of a sphere as a function of the width of the deformation, for  $\ell = 1 - 5$ . These corrections increase monotonically both in the width of the bump and in the order of the eigenfunction. (Right) First-order Laplacian eigenvalue corrections normalized by their base eigenvalue,  $\lambda_{\ell m}^{(0)}$ .

development of Turing patterns on spheres have a tendency to stabilize spotted patterns instead of the exact spherical harmonic patterns predicted by the linear analysis [18], this feature can be observed in the initial development of Turing patterns, where an inward deformation causes the most diffusively unstable mode to switch to one corresponding to a lower diffusion rate, see Fig. 4-8.

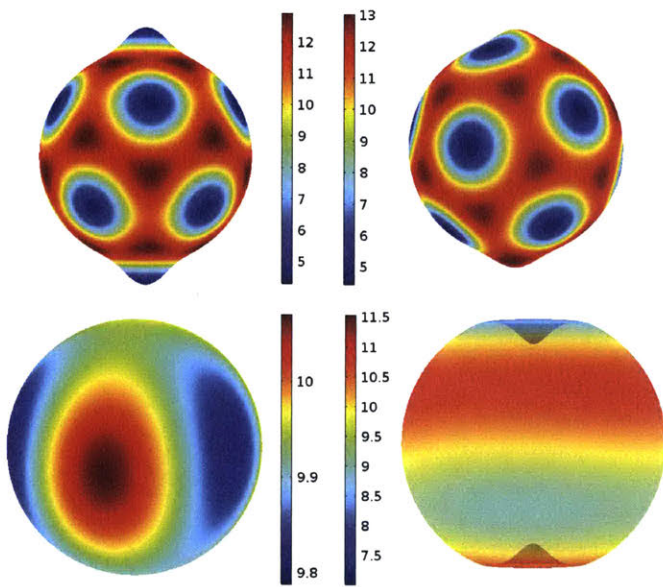


Figure 4-8: (Top) Spotted patterns from the Thomas-Murray reaction-diffusion model on deformed spheres can be entrained to deformations, possibly prevented by incommensurability of length scales and nonlinear interactions. (Bottom) In the initial development of Turing patterns, an undeformed sphere presents diffusionally-unstable modes corresponding to the eigenfunction  $Y_5^5$ . Upon introducing inward deformations, the diffusion rate of lower harmonics is increased, thus causing the  $Y_3^0$  pattern to become diffusionally unstable.



# Chapter 5

## Time-Dependent Turing Patterns

### 5.1 Introduction to Reaction-Advection-Diffusion Systems

Many physical systems can be modeled by the reaction-diffusion system outlined in Chapter 2. However, a more general equation of motion can be obtained by including *advection*,

$$\frac{\partial \mathbf{C}}{\partial t} = \mathbf{D} \Delta \mathbf{C} + \mathbf{a} \cdot \nabla \mathbf{C} + R(\mathbf{C}) \quad (5.1)$$

Advection is used to describe transport of a substance, with the speed and direction characterized by  $\mathbf{a}$ , and plays a role in physical processes ranging from population dynamics [35] to biological tissues [36]. Eq. 5.1 is known as the reaction-advection-diffusion equation<sup>1</sup> and can possess instabilities; i.e., there exist perturbations around a homogeneous solution whose time evolution is governed by  $e^{\omega t}$ , where  $\text{Re}(\omega) > 0$ . However, unlike reaction-diffusion equations,  $\omega$  can take on complex values, indicating periodic time evolution. When the resulting patterns are also periodic in space, this leads to traveling waves, or Turing patterns propagating across the surface [17, 37, 38].

As a first pass, one might expect curvature to modify how time-dependent Turing

---

<sup>1</sup>Rather, there are  $3!$  possible titles for this equation, depending on how the authors choose to permute the three terms. Luckily, standard search engines are indifferent to this ordering.

patterns move across surfaces, potentially changing the velocity of the patterns. In this section, we study this hypothesis. After summarizing the behavior of reaction-advection-diffusion equations on surfaces of uniform curvature, we outline the mathematical barriers in analytically studying these equations on curved surfaces. We conclude with a preliminary numerical study of these time-dependent Turing patterns which, despite not being as comprehensive as other numerical studies in this thesis, suggests a curvature-dependent velocity.

## 5.2 Linear Stability Analysis of Reaction-Advection-Diffusion Systems

Mirroring the analysis carried out in Chapter 2, we conduct a linear stability analysis of reaction-advection-diffusion systems and examine the instabilities. Unlike Chapter 2, the below analysis is not valid for general surfaces - for reasons specified later in this section, it becomes necessary to make an assumption which only holds for a class of geometries which includes cylinders, spheres, and flat planes. Furthermore, we consider the concrete case of an undeformed cylinder with advection along the length of the cylinder, as maintaining a more general notation forfeits conceptual clarity. This linear analysis mirrors the derivations carried out in [39].

We begin with the reaction-advection-diffusion equation specified in Eq. 5.1, with the definitions

$$\mathbf{C}(\mathbf{r}, t) = \begin{pmatrix} C_1(\mathbf{r}, t) \\ C_2(\mathbf{r}, t) \end{pmatrix}, \quad \mathbf{D} = \begin{pmatrix} 1 & 0 \\ 0 & \beta \end{pmatrix}, \quad \mathbf{a}_z = \begin{pmatrix} a_1 & 0 \\ 0 & a_2 \end{pmatrix}.$$

Let us consider perturbations  $\mathbf{c}(\mathbf{r}, t)$  around a homogeneous steady-state solution, and decompose the perturbations into simultaneous eigenfunctions of both the diffusion and advection operator. Note that this assumes that the advection and diffusion operator share a common basis of eigenfunctions, which we will find later is *not* true generally. However, this assumption does hold for the case currently under consider-

ation, as well as spheres and flat planes.

Using the notation for the eigenfunctions of a flat cylinder specified in Eq. 4.2, we find that each mode  $\tilde{\mathbf{c}}_k$  satisfies

$$\frac{\partial \tilde{\mathbf{c}}_k}{\partial t} = \begin{pmatrix} -(\bar{k}^2 + \bar{s}^2) + ia_1\bar{k} + M_{11} & M_{12} \\ M_{21} & -\beta(\bar{k}^2 + \bar{s}^2) + ia_2\bar{k} + M_{22} \end{pmatrix} \tilde{\mathbf{c}}_k \quad (5.2)$$

By shifting to a moving frame along the length of the cylinder,  $z \rightarrow z + vt$ , the advection coefficients also become shifted by  $v$ . As such, one can shift to a moving frame where  $a_1 = \tilde{a} = -a_2$ , which simplifies analysis.

In this frame, eigenfunctions of the RHS of Eq. 5.2 satisfy

$$\begin{aligned} \omega^2 + \alpha_1\omega + \alpha_0 &= 0, \\ \alpha_1 &= (1 + \beta)k^2 - M_{11} - M_{22}, \\ \alpha_0 &= (-k^2 + i\tilde{a}k + M_{11})(-\beta k^2 - i\tilde{a}k + M_{22}) - M_{21}M_{12}. \end{aligned} \quad (5.3)$$

The requirement for a diffusional instability to be present,  $\text{Re}(\omega) > 0$ , is

$$\alpha_1^2 \text{Re}(\alpha_0) - \text{Im}(\alpha_0)^2 > 0 \quad (5.4)$$

This reduces to the standard condition for diffusional instability when  $\tilde{a} = 0$ , but a non-zero  $\tilde{a}$  can modify these conditions, indicating that instabilities can be driven by advection differences between the two concentrations.

With the introduction of advection,  $\omega$  is no longer strictly real. The imaginary portion of  $\omega$  causes resulting Turing patterns to move in the direction of advection, with velocity  $\text{Im}(\omega)/k$ . The velocity of the critical eigenvalue, where  $\text{Re}(\omega) = 0$ , is expressed in more fundamental terms as

$$\frac{\text{Im}(\omega)}{k} = \frac{1}{2}(a_1 + a_2) - \frac{(a_1 - a_2)[(1 - \beta)k^2 + M_{22} - M_{11}]}{2(1 + \beta)k^2 - M_{11} - M_{22}} \quad (5.5)$$

Naturally, if  $a_1 = a_2 = a$ , the second term vanishes and the velocity of the resulting patterns is simply  $a$ .

## 5.3 Conformal Mapping the Advection Operator

The approach for studying reaction-advection-diffusion equations on curved surfaces remains the same as what was developed in the previous chapter, with the caveat that now we must understand how the advection operator transforms under conformal mappings. Once again, we take our conformal mapping to be

$$G_{ab} \equiv \Omega^2 g_{ab} \quad (5.6)$$

with coordinate systems  $x^i$  and  $u^i$ , respectively. Each component of the advection operator - the gradient - satisfies

$$\nabla_G^i \phi = G^{ij} \frac{\partial \phi}{\partial x^j} \quad (5.7)$$

Rewriting this using Eq. 5.6 and the chain rule, we obtain

$$\nabla_G^i \phi = \frac{1}{\Omega^2} g^{ij} \frac{\partial \phi}{\partial x^j} = \frac{1}{\Omega^2} g^{ij} \frac{\partial \phi}{\partial u^k} \frac{\partial u^k}{\partial x^j} = \frac{1}{\Omega^2} \frac{\partial u^i}{\partial x^j} \nabla_g^j \phi \quad (5.8)$$

The last step in this derivation makes two assumptions - that the metric  $g^{ij}$  is diagonal, and that the Jacobian  $\frac{\partial u^k}{\partial x^j}$  is diagonal. These assumptions hold true for all the cases previously considered, and also hold true in a respectable number of other cases. The latter assumption tends to not hold for non-symmetric deformations, such as a deformation of a cylinder without radial symmetry, but even in these cases, the gradient operator is still well-defined in the conformal coordinates.

## 5.4 Advection on a Deformed Cylinder

### 5.4.1 Analytical Restrictions

Having outlined how the advection operator transforms generally, we study the effects of advection along the length of a deformed cylinder, again with length  $L$  and radius  $R_0$ . To first order, the gradient along the length of a deformed cylinder in conformally

flat coordinates is given by

$$\nabla_G^z \phi = \frac{1}{\Omega^3} \nabla_g^v \phi \quad (5.9)$$

This indicates that a more complicated analysis than before will be necessary, as  $\nabla_G^z$  and  $\Delta^G$  no longer commute. Specifically, for deformations from a cylinder,

$$[\nabla_G^z, \Delta^G] = -4h_v \frac{\partial^2}{\partial v^2} - 3h_{vv} \frac{\partial}{\partial v} \quad (5.10)$$

This means that we can no longer decompose our chemical concentrations into simultaneous eigenfunctions of both the advection and diffusion operator. Moreover, the full advection-diffusion operator

$$-\eta \Delta^G + a \nabla_G^z \quad (5.11)$$

is not normal at  $\mathcal{O}(\epsilon)$  - it does not commute with its Hermitian conjugate. This means that one cannot assume that Eq. 5.11 has an orthogonal basis over our Hilbert space, and perturbation theory breaks down. As a result, analytically studying the effects of non-uniform curvature on advection-diffusion systems, at least in this subset of systems, appears intractable<sup>2</sup>.

### 5.4.2 Numerical Results

Despite the difficulties in analytically studying systems involving both diffusion and advection on deformed surfaces, numerical simulations can still be carried out using COSMOS Multiphysics®. We carry out simulations of a reaction-advection-diffusion system with  $a_1 = a_2 = 0.05$  on a cylinder with a Gaussian deformation, and plot the dependence of the velocity of the pattern as a function of  $\epsilon$  and  $\sigma$  in Fig. 5-1. These simulations indicate not only that non-uniform curvature can modify the velocity at which Turing patterns propagate, but these modifications are sensitive to the sign of the curvature - an inward deformation appears to speed up pattern

---

<sup>2</sup>One should note that such a study is tractable if one considers advection in the angular direction as opposed to along the length of the cylinder. However, advection in this direction does not lead to time-dependent Turing patterns when considering striped patterns.

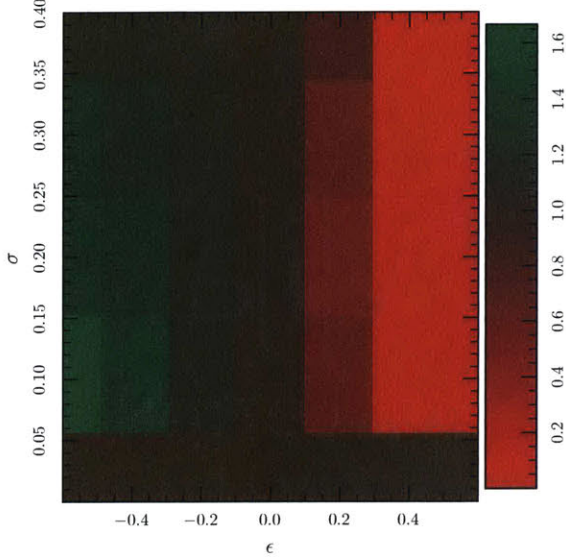


Figure 5-1: The velocity of the propagation of Turing patterns in a reaction-advection-diffusion system on a deformed cylinder, normalized by the advection rate  $a_1 = a_2 = a$ . Inward Gaussian deformations speed up the rate of propagation, whereas outward Gaussian deformations slow it down, potentially stopping the flow of the pattern all together. A slight dependence on the width of the deformation  $\sigma$  is also observed, suggesting that deformations with larger curvature modify propagation speed more.

movement, whereas an outward deformation slows it down. Moreover, for sufficiently large deformations, the patterning becomes fixed to a stationary solution. This is a noteworthy result in regards to physical systems, as it provides a mechanism by which stationary patterns can be stable against small amounts of advection. This sensitivity to non-uniform curvature becomes less pronounced for larger advection terms, and becomes negligible for  $a = 0.01$  in the regime graphed in Fig. 5-1.

# Chapter 6

## Conclusion

The Turing mechanism provides a general framework for modeling pattern formation in a diverse set of chemical and biological systems. Although the geometric dependence of these patterns is manifest in the underlying reaction-diffusion equations, understanding how non-uniform curvature affects pattern formation is not immediately obvious. In this thesis, we have developed a framework, using conformal mappings to express geometric effects perturbatively, for studying the behavior of reaction-diffusion equations in the presence of small geometric deformations from surfaces of uniform curvature. With this, we analytically and numerically observe two clear effects on pattern formation - symmetry breaking and the modification of the stability conditions. In cases where analytic results become unobtainable, numerical simulations are able to show further consequences of non-uniform curvature; namely, pattern localization and the modification of the velocity of propagating Turing patterns. These advances suggest that non-uniform curvature may play a role in pattern formation in chemical and biological systems, and moreover, may be studied analytically in a wide variety of cases.



# Appendix A

## Rayleigh-Schrödinger Perturbation Theory for Momentum-Dependent Potentials

### A.1 Problem Statement

In analyzing geometric modifications to Laplacian eigenfunctions, we are often faced with perturbatively studying solutions of the equation

$$\left[ \hat{H}_0 + \epsilon \lambda_i \hat{V} \right] |\phi_i\rangle = \lambda_i |\phi_i\rangle \quad (\text{A.1})$$

where  $H_0$  is a Hermitian operator whose spectrum is well understood (in our case, the Laplacian operator on a standard surface), and  $\epsilon$  is our perturbation parameter. For the purpose of clearly differentiating coefficients from states, we adopt the Dirac bra-ket notation standard in quantum mechanics. We begin with the ansatz

$$\begin{aligned} \lambda_i &= \lambda_i^{(0)} + \lambda_i^{(1)} + \lambda_i^{(2)} + \dots \\ |\phi_i\rangle &= |\phi_i^{(0)}\rangle + |\phi_i^{(1)}\rangle + |\phi_i^{(2)}\rangle + \dots \end{aligned} \quad (\text{A.2})$$

where  $\hat{H}_0 \left| \phi_i^{(0)} \right\rangle = \lambda_i^{(0)} \left| \phi_i^{(0)} \right\rangle$ , and the notation  $x^{(n)}$  indicates that the expression is  $\mathcal{O}(\epsilon^n)$ . The form of the coefficients in Eq. A.2 are well-understood when our perturbation potential is independent of  $\lambda$  [40]; however, a consistent perturbation theory may still be developed in the case of  $\lambda$ -dependent perturbations.

## A.2 First Order Corrections

### A.2.1 Non-Degenerate Perturbation Theory

We proceed by analyzing Eq. A.1 and imposing equality at all orders of  $\epsilon$ . The zeroth order expression is simply the unperturbed eigenvalue equation, which is by definition satisfied. The terms first order in  $\epsilon$  give

$$\hat{H}_0 \left| \phi_i^{(1)} \right\rangle + \epsilon \lambda_i^{(0)} \hat{V} \left| \phi_i^{(0)} \right\rangle = \lambda_i^{(0)} \left| \phi_i^{(1)} \right\rangle + \lambda_i^{(1)} \left| \phi_i^{(0)} \right\rangle \quad (\text{A.3})$$

Multiplying both sides by  $\left\langle \phi_i^{(0)} \right|$  gives the explicit expression for  $\lambda_i^{(1)}$ ,

$$\lambda_i^{(1)} = \epsilon \lambda_i^{(0)} \left\langle \phi_i^{(0)} \right| \hat{V} \left| \phi_i^{(0)} \right\rangle \quad (\text{A.4})$$

We calculate first order eigenfunction corrections through the resolution of the identity,

$$\begin{aligned} \epsilon \lambda_i^{(0)} \hat{V} \left| \phi_i^{(0)} \right\rangle &= \left( \sum_{j \neq i} \left| \phi_j^{(0)} \right\rangle \left\langle \phi_j^{(0)} \right| \right) \epsilon \lambda_i^{(0)} \hat{V} \left| \phi_i^{(0)} \right\rangle + \left| \phi_i^{(0)} \right\rangle \left\langle \phi_i^{(0)} \right| \epsilon \lambda_i^{(0)} \hat{V} \left| \phi_i^{(0)} \right\rangle \\ &= \left( \sum_{j \neq i} \left| \phi_j^{(0)} \right\rangle \left\langle \phi_j^{(0)} \right| \right) \epsilon \lambda_i^{(0)} \hat{V} \left| \phi_i^{(0)} \right\rangle + \lambda_i^{(1)} \left| \phi_i^{(0)} \right\rangle \end{aligned} \quad (\text{A.5})$$

Plugging this into Eq. A.3 allows us to determine first-order eigenfunction corrections

$$\left| \phi_i^{(1)} \right\rangle = \sum_{j \neq i} \frac{\epsilon \lambda_i^{(0)} \left\langle \phi_j^{(0)} \right| \hat{V} \left| \phi_i^{(0)} \right\rangle}{\lambda_i^{(0)} - \lambda_j^{(0)}} \left| \phi_j^{(0)} \right\rangle \quad (\text{A.6})$$

### A.2.2 Degeneracy Effects

The above analysis is valid for a non-degenerate spectrum. However, issues arise when our unperturbed spectrum is degenerate, as there is ambiguity in which basis states to choose. Furthermore, the first-order eigenfunction corrections given in Eq.A.6 become infinite with a degenerate spectrum.

Dealing with these degeneracies is no different than the standard approach used without momentum-dependent potentials. For the degenerate subspace  $D$ , we choose a set of basis functions that diagonalize  $\hat{V}$  within this subspace, i.e.

$$\left\langle \phi_i^{(0)} \right| \hat{V} \left| \phi_j^{(0)} \right\rangle = 0 \text{ for } i \neq j, \quad \left| \phi_i^{(0)} \right\rangle, \left| \phi_j^{(0)} \right\rangle \in D$$

With this proper choice of basis, one can apply methods of the previous section to calculate first-order eigenfunction and eigenvalue corrections.

## A.3 Higher Order Corrections

Similar to first order corrections, higher order corrections can be carried out analogous to standard perturbation theory. However, extra care must be given towards the momentum-dependence of the potential, as this introduces new terms at higher order which lead to additional correction terms. For example, second order eigenvalue corrections are given by

$$\lambda_i^{(2)} = \epsilon^2 \sum_{j \neq i} \frac{\left| \lambda_i^{(0)} \left\langle \phi_j^{(0)} \right| \hat{V} \left| \phi_i^{(0)} \right\rangle \right|^2}{\lambda_i^{(0)} - \lambda_j^{(0)}} + \epsilon \lambda_i^{(1)} \left\langle \phi_i^{(0)} \right| \hat{V} \left| \phi_i^{(0)} \right\rangle \quad (\text{A.7})$$

where the second term is not present in standard perturbation theory.



## Appendix B

# Details of Numerical Simulations

All simulations presented in this thesis were carried out using COMSOL Multiphysics®, which uses the Finite Element Method [41] to numerically solve PDEs. COMSOL additionally uses mesh generation to model the geometric surfaces of interest.

Each simulation consisted of solving the Thomas-Murray model,

$$\begin{aligned}\frac{\partial C_1}{\partial t} &= \eta_1 \Delta^G C_1 + \gamma \left( u_{10} - C_1 - \frac{\rho C_1 C_2}{1 + C_1 + C_1^2/K} \right) \\ \frac{\partial C_2}{\partial t} &= \eta_2 \Delta^G C_2 + \gamma \left( \alpha (u_{20} - C_2) - \frac{\rho C_1 C_2}{1 + C_1 + C_1^2/K} \right)\end{aligned}\tag{B.1}$$

through the Finite Element Method on a geometry defined through COMSOL's meshing software. The parameters used in each of the simulations are listed below. When relevant, the geometric parameters used for the simulations - defined in their corresponding sections - are also specified. Note that some parameters, while defined by the same variable, have different connotations depending on the geometry. We also omit the values  $\eta_1 = 1$ ,  $u_{10} = 92$ ,  $u_{20} = 64$ ,  $\alpha = 1.5$ , and  $K = 0.1$ , as these values are constant across all simulations.

Simulation	$\eta_2$	$\gamma$	$\rho$	$R_0$	$L$	$\sigma$	$p$	$v_0$	$\epsilon$
Fig. 4-2 (top left)	9.6	2	18.5	9.8	N/A	0.1	N/A	1	N/A
Fig. 4-2 (top right)	9.6	2	18.5	9.8	N/A	0.1	N/A	1	N/A
Fig. 4-2 (bottom left)	10	2	19.3	9.8	N/A	0.1	N/A	1	N/A
Fig. 4-2 (bottom right)	10	2	19.3	9.8	N/A	0.1	N/A	1	N/A
Fig. 4-3 (top)	10	2	18.5	0.5	20	0.54	N/A	N/A	0.4
Fig. 4-3 (bottom)	10	2	18.5	0.5	20	0.54	N/A	N/A	-0.4
Fig. 4-6 (top)	10	2	18.5	1	30	N/A	8	N/A	0.2
Fig. 4-6 (bottom)	10	2	18.5	1	30	N/A	8	N/A	0.2
Fig. 4-5 (top)	10	2	19.3	0.5	30	0.77	8	N/A	1.6
Fig. 4-5 (bottom)	10	2	19.3	0.5	30	0.77	8	N/A	1.6
Fig. 4-8 (top left)	10	2	18.5	5	N/A	0.125	N/A	N/A	0.03
Fig. 4-8 (top right)	10	2	18.5	5	N/A	0.125	N/A	N/A	0.04
Fig. 4-8 (bottom left)	10	0.5	18.5	5	N/A	0.125	N/A N/A		-0.05
Fig. 4-8 (bottom right)	10	0.5	18.5	5	N/A	0.125	N/A	N/A	-0.4

Table B.1: A list of parameters used in the numerical simulations included in this thesis.

# Bibliography

- [1] Miao Jin, Yalin Wang, Shing Tung Yau, and Xianfeng Gu. Optimal global conformal surface parameterization. In H. Rushmeier, G. Turk, and J.J. Wijk, editors, *IEEE Visualization 2004 - Proceedings, VIS 2004*, pages 267–274, 2004.
- [2] A. M. Turing. The chemical basis of morphogenesis. *Philosophical Transactions of the Royal Society of London. Series B, Biological Sciences*, 237(641):37–72, 1952.
- [3] V. Castets, E. Dulos, J. Boissonade, and P. De Kepper. Experimental evidence of a sustained standing Turing-type nonequilibrium chemical pattern. *Phys. Rev. Lett.*, 64:2953–2956, Jun 1990.
- [4] István Lengyel and Irving R. Epstein. Modeling of Turing structures in the Chlorite—Iodide—Malonic acid—starch reaction system. *Science*, 251(4994):650–652, 1991.
- [5] J.D. Murray. A pre-pattern formation mechanism for animal coat markings. *Journal of Theoretical Biology*, 88(1):161 – 199, 1981.
- [6] Shigeru Kondo. How animals get their skin patterns: Fish pigment pattern as a live Turing wave. In Shigetada Nakanishi, Ryoichiro Kageyama, and Dai Watanabe, editors, *Systems Biology*, pages 37–46, Tokyo, 2009. Springer Japan.
- [7] Christoph A. Haselwandter, Martino Calamai, Mehran Kardar, Antoine Triller, and Rava Azeredo da Silveira. Formation and stability of synaptic receptor domains. *Phys. Rev. Lett.*, 106:238104, Jun 2011.
- [8] Giulio Vandin, Davide Marenduzzo, Andrew B. Goryachev, and Enzo Orlandini. Curvature-driven positioning of Turing patterns in phase-separating curved membranes. *Soft Matter*, 12:3888–3896, 2016.
- [9] Martin Baurmann, Thilo Gross, and Ulrike Feudel. Instabilities in spatially extended predator-prey systems: Spatio-temporal patterns in the neighborhood of Turing-Hopf bifurcations. *Journal of Theoretical Biology*, 245(2):220 – 229, 2007.
- [10] Yuanwei Qi and Yi Zhu. The study of global stability of a diffusive Holling-Tanner predator-prey model. *Applied Mathematics Letters*, 57:132 – 138, 2016.

- [11] Mainul Haque. Existence of complex patterns in the Beddington-DeAngelis predator-prey model. *Mathematical Biosciences*, 239(2):179 – 190, 2012.
- [12] A. A. Golovin, B. J. Matkowsky, and V. A. Volpert. Turing pattern formation in the brusselator model with superdiffusion. *SIAM Journal on Applied Mathematics*, 69(1):251–272, 2008.
- [13] Thomas Butler and Nigel Goldenfeld. Fluctuation-driven turing patterns. *Phys. Rev. E*, 84:011112, Jul 2011.
- [14] Tommaso Biancalani, Farshid Jafarpour, and Nigel Goldenfeld. Giant amplification of noise in fluctuation-induced pattern formation. *Phys. Rev. Lett.*, 118:018101, Jan 2017.
- [15] Julijana Gjorgjieva and Jon Jacobsen. Turing patterns on growing spheres: the exponential case. *Discrete Contin. Dyn. Syst.*, 2007:436–445, 2007.
- [16] C. Varea, J. L. Aragón, and R. A. Barrio. Confined Turing patterns in growing systems. *Phys. Rev. E*, 56:1250–1253, Jul 1997.
- [17] Abbey J. Pperumpanani, Jonathan A. Sherratt, and Philip K. Maini. Phase differences in reaction-diffusion-advection systems and applications to morphogenesis. *IMA Journal of Applied Mathematics*, 55(1):19–33, 1995.
- [18] R. A. Barrio, C. Varea, J. L. Aragón, and P. K. Maini. A two-dimensional numerical study of spatial pattern formation in interacting Turing systems. *Bulletin of Mathematical Biology*, 61(3):483–505, May 1999.
- [19] T. Bansagi Jr. and A. F. Taylor. Helical turing patterns in the Lengyel-Epstein model in thin cylindrical layers. *Chaos: An Interdisciplinary Journal of Nonlinear Science*, 25(6):064308, 2015.
- [20] S. Nampoothiri and A. Medhi. Role of curvature and domain shape on Turing patterns. *ArXiv e-prints*, May 2017.
- [21] Sai Yu, Hailong Wang, Yong Ni, Linghui He, Mingyuan Huang, Yuan Lin, Jin Qian, and Hongyuan Jiang. Tuning interfacial patterns of molecular bonds via surface morphology. *Soft Matter*, 13:5970–5976, 2017.
- [22] Samuel A. Ramirez, Sridhar Raghavachari, and Daniel J. Lew. Dendritic spine geometry can localize GTPase signaling in neurons. *Mol Biol Cell*, 26(22):4171–4181, Nov 2015.
- [23] Ana R. Fialho, Nelson R. Bernardino, Nuno M. Silvestre, and Margarida M. Telo da Gama. Effect of curvature on cholesteric liquid crystals in toroidal geometries. *Phys. Rev. E*, 95:012702, Jan 2017.
- [24] Suraj Shankar, Mark J. Bowick, and M. Cristina Marchetti. Topological sound and flocking on curved surfaces. *Phys. Rev. X*, 7:031039, Sep 2017.

- [25] P. W. Miller, N. Stoop, and J. Dunkel. Geometry of wave propagation on active deformable surfaces. *ArXiv e-prints*, October 2017.
- [26] Viola Vogel and Michael Sheetz. Local force and geometry sensing regulate cell functions. *Nature Reviews Molecular Cell Biology*, 7:265 EP –, Feb 2006. Review Article.
- [27] John J. Tyson, Kevin A. Alexander, V.S. Manoranjan, and J.D. Murray. Spiral waves of cyclic amp in a model of slime mold aggregation. *Physica D: Nonlinear Phenomena*, 34(1):193 – 207, 1989.
- [28] Dominik Thalmeier, Jacob Halatek, and Erwin Frey. Geometry-induced protein pattern formation. *Proceedings of the National Academy of Sciences*, 113(3):548–553, 2016.
- [29] COMSOL Multiphysics 5.2a.
- [30] E.O. Steinborn and K. Ruedenberg. Rotation and translation of regular and irregular solid spherical harmonics\*\*work was performed in part in the ames laboratory of the united states atomic energy commission. volume 7 of *Advances in Quantum Chemistry*, pages 1 – 81. Academic Press, 1973.
- [31] R.M. Schoen and S.T. Yau. *Lectures on Differential Geometry*. Conference Proceedings and Lecture Note. International Press, 1994.
- [32] A.I. Dyachenko, E.A. Kuznetsov, M.D. Spector, and V.E. Zakharov. Analytical description of the free surface dynamics of an ideal fluid (canonical formalism and conformal mapping). *Physics Letters A*, 221(1):73 – 79, 1996.
- [33] Roland Schinzingher and Patricio AA Laura. *Conformal mapping: methods and applications*. Courier Corporation, 2003.
- [34] Charles Kittel. *Introduction to Solid State Physics*. John Wiley & Sons, 2004.
- [35] G. J. Gibson, C. A. Gilligan, and A. Kleczkowski. Predicting variability in biological control of a plant—pathogen system using stochastic models. *Proceedings of the Royal Society of London B: Biological Sciences*, 266(1430):1743–1753, 1999.
- [36] Daniel A. Beard and James B. Bassingthwaighte. Advection and diffusion of substances in biological tissues with complex vascular networks. *Ann Biomed Eng*, 28(3):253–268, Mar 2000.
- [37] D.A. Garzon-Alvarado, C.H. Galeano, and J.M. Mantilla. Turing pattern formation for reaction-convection-diffusion systems in fixed domains submitted to toroidal velocity fields. *Applied Mathematical Modelling*, 35(10):4913 – 4925, 2011.

- [38] Estefania Vidal-Henriquez, Vladimir Zykov, Eberhard Bodenschatz, and Azam Gholami. Convective instability and boundary driven oscillations in a reaction-diffusion-advection model. *Chaos: An Interdisciplinary Journal of Nonlinear Science*, 27(10):103110, 2017.
- [39] E. Siero, A. Doelman, M. B. Eppinga, J. D. M. Rademacher, M. Rietkerk, and K. Siteur. Striped pattern selection by advective reaction-diffusion systems: Resilience of banded vegetation on slopes. *Chaos: An Interdisciplinary Journal of Nonlinear Science*, 25(3):036411, 2015.
- [40] D.J. Griffiths. *Introduction to Quantum Mechanics*. Cambridge University Press, 2016.
- [41] J. N. Reddy. *An Introduction to the Finite Element Method, 3rd ed.* MHS, 2006.